POLYOXOMETALATES

Open Access
RESEARCH ARTICLE

Efficient phenol-to-cyclohexanone hydrogenation enabled by hydrogen spillover in sub-nanometric Pd-polyoxovanadomolybdate catalysts

Yanchun Liu[1,2], Zixuan Liu[1], Zhongling Lang[1] ✉, Ruiqi Yao[1], Feiyang Yu[1], Aicen Li[1], Huaqiao Tan[1] ✉, and Yangguang Li[1] ✉

[1] *Key Laboratory of Polyoxometalate and Reticular Material Chemistry of Ministry of Education, Faculty of Chemistry, Northeast Normal University, Changchun 130024, China*
[2] *Engineering Research Center of Advanced Rare Earth Materials, Department of Chemistry, Tsinghua University, Beijing 100084, China*

Cite This: *Polyoxometalates*, **2026**, *5*, 9140109

Read Online

ABSTRACT: Polyoxometalate (POM)-mediated cluster catalysis has emerged as a promising strategy for the development of efficient and selective catalysts because of its unique advantages in activity modulation, interface engineering, and electron/proton transfer. In this study, a series of sub-nanowire hybrid catalysts (denoted as Pd-$PMo_{12-x}V_x$, x = 0–3) is successfully constructed via a self-assembly strategy involving Keggin-type POMs and Pd^0 clusters. Among them, Pd-$PMo_{10}V_2$ exhibits excellent catalytic performance for the selective hydrogenation of phenol to cyclohexanone, achieving 99.9% phenol conversion and 95.4% product selectivity. Experimental results demonstrate that POMs not only effectively stabilize sub-nano Pd^0 clusters but also modulate their electronic structures, thereby enhancing the catalytic activity. Compared with tungsten-based POMs, molybdenum-based analogs exhibit stronger reducibility and superior electron/proton acceptance capabilities, which provide more efficient active hydrogen transfer channels for multi-hydrogenation processes. Moreover, increasing the reaction temperature can help overcome the energy barrier associated with the electron-coupled proton transfer process, thereby enabling the full utilization of redox active sites within POMs. This work provides a novel design strategy and mechanistic insight for the development of highly active and selective noble-metal cluster catalysts.

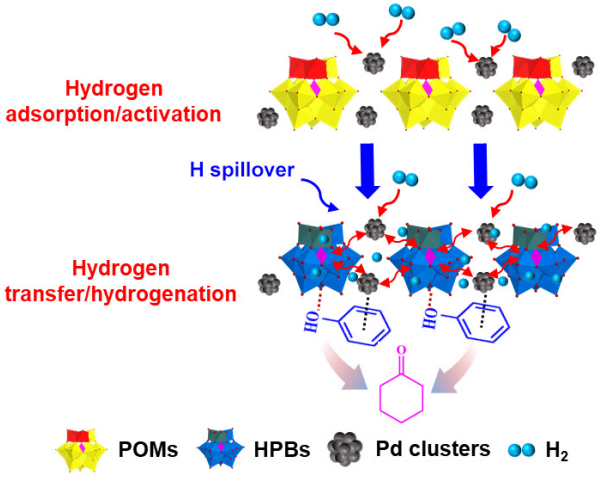

KEYWORDS: polyoxometalates, Pd clusters, selective hydrogenation, phenol, catalytic performance

1 Introduction

Lignocellulosic biomass offers a renewable feedstock for the sustainable production of fuels and chemicals [1–5]. Among products derived from lignin depolymerization, phenol stands out as a versatile platform molecule for its structural diversity and abundance [6–8]. However, its high oxygen content and intrinsic stability hinder direct fuel applications. The selective hydrogenation of phenol to cyclohexanone or cyclohexanol is a practical alternative, affording intermediates of considerable industrial relevance [9]. Notably, cyclohexanone is a key precursor for caprolactam and adipic acid—the monomers of nylon-6 and nylon-6,6—and serves as a widely used solvent in coatings, adhesives, and resins [10–12]. Accordingly, the development of efficient catalytic systems with high selectivity toward cyclohexanone in phenol hydrogenation holds both fundamental and practical significance.

The selective hydrogenation of phenol to cyclohexanone involves a four-electron/proton transfer process that demands a high concentration of active hydrogen species [13, 14]. However, excessive hydrogen coverage on the catalyst surface inevitably drives over-hydrogenation to cyclohexanol, thereby compromising selectivity [15, 16]. To resolve this intrinsic issue, designing efficient interfacial hydrogen transport pathways that alleviate surface hydrogen accumulation while facilitating continuous H^* migration is crucial [17, 18]. Polyoxometalates (POMs), a class of discrete metal–oxygen clusters with well-defined structures, reversible redox properties, and tunable acidity, offer unique opportunities in this

Received: November 26, 2025; **Revised:** December 19, 2025
Accepted: December 25, 2025

✉Address correspondence to Zhongling Lang, langzl554@nenu.edu.cn; Huaqiao Tan, tanhq870@nenu.edu.cn; Yangguang Li, liyg658@nenu.edu.cn

https://doi.org/10.26599/POM.2026.9140109

context [19–27]. Specifically, their oxygen-rich surfaces and highly negative charges can not only stabilize ultra-small noble-metal clusters and regulate their electronic structures but also provide ideal channels for active hydrogen species transport [28–35]. In our recent study, we successfully constructed two Pd^0-POM cluster catalysts that demonstrated remarkable efficiency in selective olefin hydrogenation [36]. The detailed mechanistic studies revealed that its catalytic behavior is mainly governed by three key steps: (i) dissociation of H_2 on Pd clusters, (ii) hydrogen spillover between Pd clusters and POMs, and (iii) selective adsorption and activation of substrates at the Pd–POM interface. The hydrogen spillover step plays a central role. Active hydrogen generated by Pd clusters can be transferred to the redox centers of POMs through spillover and released back to the catalytic interface when needed for the reaction [37–39]. This dynamic storage and redistribution process effectively regulates the hydrogen coverage on the Pd surface, ensuring a sufficient supply of active hydrogen and avoiding the generation of byproducts induced by excessive hydrogenation. Notably, molybdenum-based POMs possess stronger hydrogen storage ability than tungsten-based analogs, providing more efficient active hydrogen transfer channels for multi-hydrogenation processes. Inspired by the high negative charge, strong reducibility, and intrinsic catalytic activity of phosphovanadomolybdate POMs [40–42], their rational integration with active Pd clusters might offer a versatile platform to modulate electronic structure and hydrogen binding affinity and hence steer phenol hydrogenation toward cyclohexanone with high efficiency and selectivity.

In this study, a series of dual-confinement Pd–POM catalysts is constructed via strong interfacial coordination between sub-nanometer Pd^0 clusters and $PMo_{12-x}V_x$ (denoted as Pd-$PMo_{12-x}V_x$, x = 0–3). Comprehensive characterizations confirm the quasi-monodisperse distribution of Pd clusters around the $PMo_{12-x}V_x$ surface and the formation of a well-defined catalytic interface. Among them, Pd-$PMo_{10}V_2$ exhibits outstanding catalytic activity for selective phenol hydrogenation: Complete phenol conversion (99.9%) and high cyclohexanone selectivity (95.4%) are achieved within 5 h under mild conditions (60 °C and 1.0 MPa of 20% H_2/N_2). Moreover, the catalyst demonstrates excellent recyclability with negligible changes in morphology and performance after multiple cycles. Mechanistic studies reveal a multilevel synergistic effect between Pd^0 clusters and POMs, where Pd^0 sites are responsible for activating H_2 molecules while $PMo_{12-x}V_x$ stabilizes the clusters and mediates electron–proton transfer. In addition, vanadomolybdate-based POMs with low redox potential promote hydrogen spillover, particularly at high temperatures. Overall, this study presents rationally designed Pd-$PMo_{12-x}V_x$ cluster–cluster catalysts with high activity and selectivity for phenol hydrogenation, providing valuable insights into the interfacial electron-coupled proton transfer and a general strategy for advanced catalyst development.

2 Experimental

2.1 Materials

Phosphotungstic acid ($H_3PW_{12}O_{40}$, PW_{12}), phosphomolybdic acid ($H_3PMo_{12}O_{40}$, PMo_{12}), sodium metavanadate ($NaVO_3$), disodium hydrogen phosphate (Na_2HPO_4), disodium molybdate ($NaMoO_4{\cdot}2H_2O$), palladium acetylacetonate ($Pd(acac)_2$), oleic acid (OA), and oleylamine (OAm) were purchased from Beijing Reagent. Phenol, cyclohexanone, cyclohexanol, cyclohexane, p-cresol, m-cresol, o-cresol, 4-chlorophenol, 4-methoxyphenol, n-hexane, ethanol, toluene, acetonitrile, and ethyl acetate were obtained from Aladdin Scientific Co., Ltd. Concentrated sulfuric acid (H_2SO_4) was purchased from Sinopharm Chemical Reagent Co., Ltd. A mixture of 20% H_2/N_2 gas was supplied by Changchun Juyang Gas Co., Ltd. $H_4PMo_{11}V_1O_{40}$ ($PMo_{11}V_1$), $H_5PMo_{10}V_2O_{40}$ ($PMo_{10}V_2$), $H_6PMo_9V_3O_{40}$ (PMo_9V_3), and $H_7PMo_8V_4O_{40}$ (PMo_8V_4) were synthesized according to a previous study [43]. All reagents were used as received without further purification, unless otherwise stated.

2.2 Synthesis of Pd-$PMo_{12-x}V_x$ catalysts (x = 0, 1, 2, and 3)

Pd-$PMo_{12-x}V_x$ catalysts were prepared using a solvothermal method. The synthesis of Pd-$PMo_{10}V_2$ is considered an example for a detailed illustration. The specific experimental steps are as follows: 18.6-mg $PMo_{10}V_2$ and 15.5-mg $Pd(acac)_2$ were added to 5.0-mL toluene and dispersed evenly under ultrasound. Then, they were transferred into a 20-mL Teflon-lined autoclave. Subsequently, 7.5-mL OA and 0.5-mL OAm were added to the mixture, and the solution was stirred for 20 min. Next, the autoclave was sealed and kept at 120 °C for 2 h. After the autoclave was cooled to room temperature, the catalysts were collected by centrifugation and washed with cyclohexane and ethanol three times. Finally, the catalysts were dried overnight in a vacuum oven (60 °C). The synthesis processes of Pd-PMo_{12}, Pd-$PMo_{11}V_1$, and Pd-PMo_9V_3 were similar to that of Pd-$PMo_{10}V_2$, where the masses of Pd-PMo_{12}, Pd-$PMo_{11}V_1$, and Pd-PMo_9V_3 were 18.0, 16.5, and 19.2 mg, respectively. For catalytic performance comparison, the Pd-PW_{12} was synthesized according to our previous study [36].

2.3 Evaluation of catalytic performance

The selective phenol hydrogenation reaction was performed in a 100-mL stainless-steel autoclave. Specifically, 10-mg catalyst, 0.5-mmol phenol, and 10-mL n-hexane were added to the autoclave and sealed. The autoclave was flushed with 0.5 MPa of 20 % H_2/N_2 five times and pre-heated for 10 min in a water bath (60 °C). Then, the autoclave was charged to 1.0 MPa of 20% H_2/N_2 and stirred at a speed of 800 rpm. After the reaction was completed, the reaction solution was centrifuged and washed with n-hexane. The phenol conversion rate and product selectivity were analyzed via gas chromatography (GC, Agilent 7820) equipped with a capillary column of 123-5532UI (30 m × 0.32 mm × 0.25 μm). The detailed analysis conditions of GC are as follows: the inlet temperature was 260 °C; the flame ionization detector (FID) temperature was 300 °C; the initial column box temperature was 80 °C, which was held for 2 min and increased to 260 °C with a heating rate of 10 °C·min^{-1}. The phenol conversion rate and product selectivity were calculated as follows:

$$\text{Conversion} = \left(1 - \frac{\text{molesofphenol}}{\text{molesofphenol, cyclohexanoneandcyclohexanol}}\right) \times 100\% \quad (1)$$

$$\text{Selectivity of cyclohexanone} = \frac{\text{moles of cyclohexanone}}{\text{moles of cyclohexanone and cyclohexanol}} \times 100\% \quad (2)$$

$$\text{Selectivity of cyclohexanol} = \frac{\text{moles of cyclohexanol}}{\text{moles of cyclohexanone and cyclohexanol}} \times 100\% \quad (3)$$

2.4 Characterization

Powder X-ray diffractometry (PXRD) was conducted on a Bruker AXS D8 Focus with filtered Cu Kα radiation (λ = 1.5418 Å). Small-angle X-ray powder diffraction (SXRD) measurements were performed with 2θ scans between 1° and 10° at a speed of 0.5 °·min^{-1}. Fourier transform infrared (FTIR) spectra were obtained using a Nicolet iS10 FTIR spectrometer with potassium bromide (KBr) as the reference. Raman spectra were examined on a Renishaw Invia confocal microscope with an excitation laser of 532 nm. Transmission electron microscopy (TEM) and high-resolution TEM (HRTEM) images were obtained using a JEOL JEM-2010 instrument with an accelerating voltage of 200 kV. X-ray photoelectron spectroscopy (XPS) was performed using an ESCALABMKII spectrometer with an Al-Kα achromatic X-ray source. All XPS spectra were corrected with the C 1s peak at 284.8 eV. Thermogravimetric analysis (TGA) curves were obtained using a Diamond TG/DTA/DSC Thermal Analyzer System (Perkin-Elmer, USA) with a heating rate of 10 °C·min^{-1} to 800 °C under N_2 atmosphere. Solid-state ^{31}P nuclear magnetic spectroscopy (^{31}P NMR) measurements were performed on a Bruker Avance III spectrometer. Inductively coupled plasma atomic emission spectrometry (ICP-AES) was performed using a Prodigy Leeman spectrometer. Hydrogen temperature programmed desorption (H_2-TPD) curves were obtained on a Micromeritics AutoChem II 2920 using a thermal conductivity detector.

3 Results and discussion

3.1 Synthesis and characterization of Pd–POM cluster–cluster catalysts

As shown in Fig. 1(a), a series of Pd–POM cluster catalysts (abbreviated as Pd-$PMo_{12-x}V_x$, x = 0–3) were synthesized using a solvothermal method with $Pd(acac)_2$, POMs, OA, and OAm as precursors. POMs play a crucial role in directing the formation of the catalysts. The oxygen-rich surface and highly negative charges of POMs induce the slow nucleation and controlled aggregation of Pd^{2+}, ultimately forming Pd clusters stabilized by OA and OAm molecules. The resulting catalysts exhibit similar morphologies and structures; Pd-$PMo_{10}V_2$ demonstrates the best catalytic performance and is hence selected for detailed characterization. Controlled experiments reveal that only irregular Pd nanoparticles can be formed without $PMo_{10}V_2$ (Fig. S1 in the Electronic Supplementary Material (ESM)). Meanwhile, nanobelts assembled by regularly aligned nanowires are obtained in the absence of $Pd(acac)_2$ (Fig. S2 in the ESM). These results confirm that $PMo_{10}V_2$ functions as templates or multi-dentate ligands to form such cluster catalysts. In addition, the synthesis temperature and OAm/OA ratio considerably affect the regular arrangement of the cluster catalysts. An increase in temperature or OAm proportion accelerates the nucleation and growth of Pd species, which hinders the formation of well-defined cluster catalysts (Figs. S3 and S4 in the ESM).

TEM image reveals that Pd-$PMo_{10}V_2$ exhibits a well-defined nanobelt morphology comprising regularly aligned nanowires (Fig. 1(b)). As shown in Fig. 1(c), the nanowires possess an average diameter of ~ 1 nm, which closely matches the molecular size of the

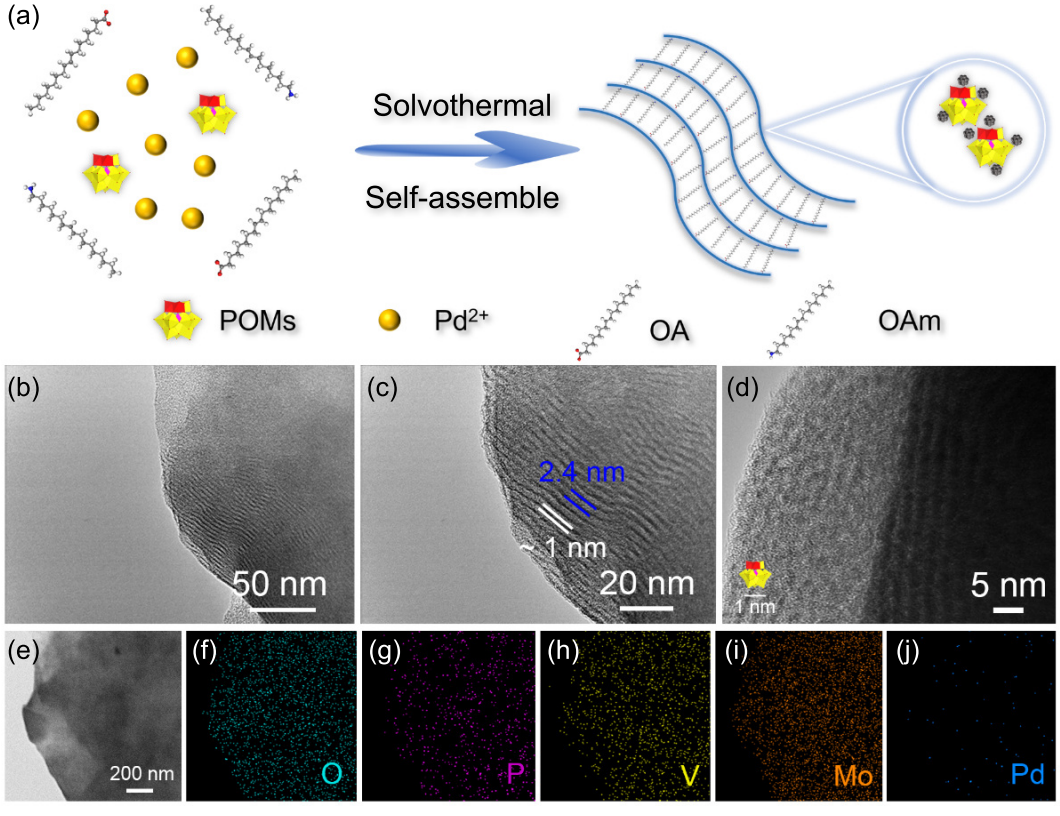

Figure 1 (a) The synthesis schematic diagram of Pd-POMs catalysts. (b) and (c) TEM images, (d) HRTEM image, and (e)–(j) elemental mapping images of Pd-$PMo_{10}V_2$, respectively.

$PMo_{10}V_2$ cluster. The spacing between nanowires is measured to be ~ 2.4 nm, slightly longer than the lengths of OA and OAm molecules (~ 2.2 nm), indicating that the nanowires are encapsulated and stabilized by the surfactants through supramolecular interaction [44]. HRTEM image confirms the homogeneous dispersion of $PMo_{10}V_2$ cluster within Pd-$PMo_{10}V_2$ (Fig. 1(d)). The elemental mapping images (Figs. 1(e)–1(j)) demonstrate that O, P, V, Mo, and Pd are uniformly distributed over Pd-$PMo_{10}V_2$, verifying the compositional homogeneity of the hybrid material. In addition, quantitative elemental analyses using scanning electron microscope energy dispersive X-ray (SEM-EDX) and ICP-AES further support these findings (Tables S1 and S2 in the ESM). Moreover, the TGA curves indicate a marked weight loss of 48.2% between 150 and 700 °C (Fig. S5 in the ESM), attributable to the thermal decomposition of the OA and OAm ligands.

The crystal structure and chemical composition of Pd-$PMo_{10}V_2$ were first characterized by PXRD. For pristine $PMo_{10}V_2$, four distinct diffraction peaks located at 2θ = 26.3°, 27.9°, 28.5°, and 29.0° are observed (Fig. S6 in the ESM), confirming the successful synthesis of $PMo_{10}V_2$ [45]. For Pd-$PMo_{10}V_2$, the peak intensities decrease and the characteristic diffraction peaks disappear, suggesting the homogeneous dispersion of $PMo_{10}V_2$ cluster within the hybrid material (Fig. 2(a)). Concurrently, two broad peaks appear at 2θ = 39.9° and 46.4°, corresponding to the (111) and (200) crystal planes of Pd clusters, suggesting the formation of ultra-small clusters in Pd-$PMo_{10}V_2$, consistent with previous HRTEM results [46]. SXRD pattern reveals a single peak at 2θ = 2.6°, which corresponds to an interlayer distance of ~ 3.4 nm, indicating its periodically aligned structure (Fig. 2(b)) [47]. As shown in Fig. 2(c), the FTIR spectrum of $PMo_{10}V_2$ displays four characteristic bands located at 1049, 953, 866, and 734 cm^{-1}, assigned to the P–O_a, M–O–M (corner-shared oxygen; M is the metal in $PMo_{10}V_2$), M–O_c–M (edge-shared oxygen), and M–O_d (terminal oxygen) [45, 48]. These peaks can also be observed in Pd-$PMo_{10}V_2$ but exhibit slight redshifts, suggesting that $PMo_{10}V_2$ is structurally preserved while engaging in strong interaction with Pd clusters (Fig. S7 in the ESM). In addition, vibration bands at 2852 and 2917 cm^{-1} correspond to the symmetric and asymmetric CH_3 and CH_2 stretching vibrations from OA and OAm molecules, verifying their presence as surface ligands [30]. The Raman spectra (Fig. 2(d)) confirm the structural integrity of the $PMo_{10}V_2$ cluster. The observed two obvious peaks at 249 and 980 cm^{-1} are attributed to the vibrations of ν_s(Mo–O_a) and ν_s(Mo–O_t) in $PMo_{10}V_2$, respectively, which are also present in Pd-$PMo_{10}V_2$, albeit with a shift to lower wavenumbers, reinforcing the presence of strong interactions between Pd clusters and $PMo_{10}V_2$ [49]. Solid-state ^{31}P

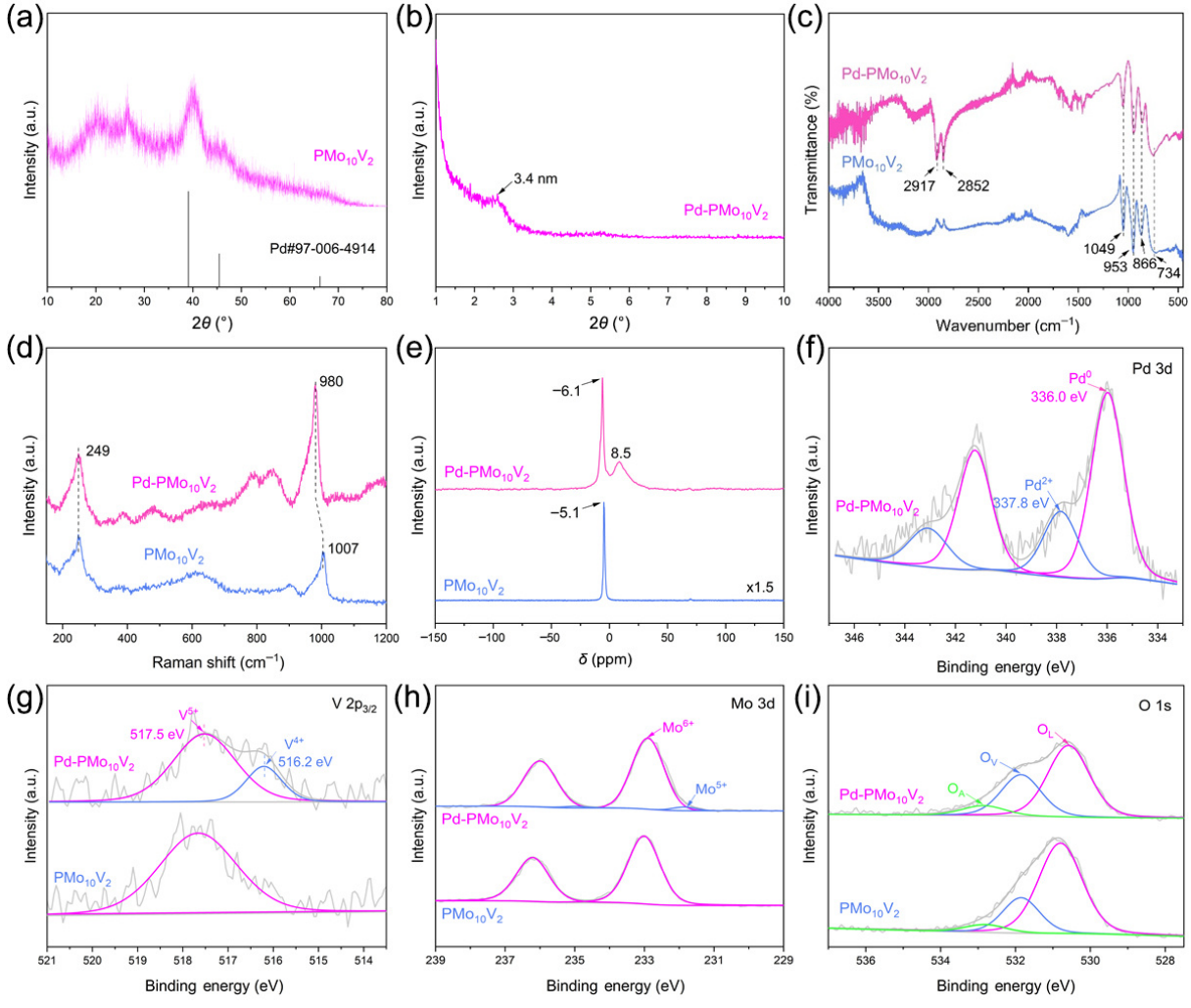

Figure 2 (a) XRD pattern and (b) SXRD pattern of Pd-$PMo_{10}V_2$. (c) FTIR spectra, (d) Raman spectra, and (e) ^{31}P NMR spectra of $PMo_{10}V_2$ and Pd-$PMo_{10}V_2$. (f) High-resolution Pd 3d XPS spectrum of Pd-$PMo_{10}V_2$. High-resolution XPS spectra of (g) V $2p_{3/2}$, (h) Mo 3d, and (i) O 1s of $PMo_{10}V_2$ and Pd-$PMo_{10}V_2$, respectively.

NMR reveals a symmetric peak at δ = −5.1 ppm for $PMo_{10}V_2$ (Fig. 2(e)). Meanwhile, Pd-$PMo_{10}V_2$ exhibits two distinct peaks at −6.1 and 8.5 ppm, attributable to ligand coordination effects from OAm/OA molecules and the strong electronic coupling between Pd clusters and $PMo_{10}V_2$, respectively. Collectively, these results confirm the structural preservation of $PMo_{10}V_2$ and reveal a robust interaction between Pd clusters and POMs, which is expected to enhance electron-coupled proton (e^- + H^+) transfer and improve catalytic hydrogenation activity.

XPS was further employed to investigate the elemental composition and valence states of the catalysts. The survey XPS spectra in Fig. S8 in the ESM confirm the presence of C, N, O, P, V, Mo, and Pd, consistent with the expected composition of Pd-$PMo_{10}V_2$. In the high-resolution Pd 3d spectrum (Fig. 2(f)), the peaks at 336.0 eV ($3d_{5/2}$) and 341.2 eV ($3d_{3/2}$) are ascribed to the metallic Pd^0 species whereas the peaks at 337.8 eV ($3d_{5/2}$) and 343.1 eV ($3d_{3/2}$) are ascribed to the Pd^{2+} species, suggesting that Pd clusters exist in a mixed-valence state, defined as $Pd^{\delta+}$ ($0 < \delta < 2$) [50]. As shown in the high-resolution V $2p_{3/2}$ spectra in Fig. 2(g), the predominant peak at 517.5 eV in pristine $PMo_{10}V_2$ corresponds to V^{5+} [51]. Notably, an additional peak at 516.2 eV is observed after the hybrid catalyst formation, indicating the partial reduction of V^{5+} to V^{4+} within the catalyst [52]. Similarly, in the high-resolution Mo 3d spectra (Fig. 2(h)), dominant peaks at 232.9 and 236.0 eV are attributed to Mo^{6+} whereas weaker peaks at 231.9 and 235.0 eV suggest the presence of a minor fraction of Mo^{5+} species [53]. As shown in Fig. 2(i), the O 1s spectra corroborate these findings, revealing three distinct oxygen environments: lattice oxygen (O_L) at 530.8 eV, oxygen vacancies (O_V) at 531.8 eV, and adsorbed oxygen species (O_A) at 532.8 eV [54]. Collectively, the appearance of oxygen vacancies and low-valence metal species confirms the partial reduction of POM clusters during the cluster catalyst formation and suggests strong electron transfer between Pd clusters and POMs, which may contribute to enhanced catalytic activity [55].

A series of POMs, including PW_{12}, PMo_{12}, and $PMo_{12-x}V_x$, were selected to verify the versatility of constructing such Pd–POM cluster catalysts using POMs as multi-dentate ligands (Fig. S9 in the ESM). The results reveal that PW_{12}, PMo_{12}, $PMo_{11}V_1$, and PMo_9V_3, which exhibit morphologies and particle sizes comparable to those of Pd-$PMo_{10}V_2$, can facilitate the formation of well-defined architectures with Pd clusters. However, Pd-PMo_8V_4 fails to form the desired structure, attributable to its intrinsic instability and diminished structural robustness under solvothermal conditions. FTIR spectra (Fig. S10 in the ESM) show the preservation of POMs in all catalysts and indicate strong interactions between Pd clusters and POMs. Complementary structural characterizations, including XRD, SXRD, and Raman spectrometry, provide sufficient evidence for the successful formation of Pd–POM cluster catalysts (Figs. S11 and S12 in the ESM). Figures S13 and S14 in the ESM show the XPS results of various Pd-POM catalysts. POMs undergo varying degrees of reduction during the catalyst formation. Notably, Mo atoms are preferentially reduced in Pd-PMo_{12} whereas V atoms exhibit great reducibility in Pd-$PMo_{12-x}V_x$ systems, consistent with their lower redox potentials. The above findings suggest that heteroatom substitution in POMs can effectively modulate their redox behaviors and electronic interactions with Pd clusters, offering a versatile platform for further tailoring catalytic properties through rational heteroatom engineering.

3.2 Selective hydrogenation activity of Pd–POM catalysts

Selective phenol hydrogenation is considered as a model reaction to evaluate the catalytic performance of various Pd–POM cluster catalysts. The proposed reaction pathway for phenol hydrogenation is shown in Fig. 3(a). Control experiments (Table S3 in the ESM) demonstrate that Pd^0 species serve as the key active sites responsible for catalytic activity. Pd-$PMo_{10}V_2$ was selected as a representative catalyst to determine the optimal reaction conditions. As shown in Fig. 3(b), phenol conversion increases progressively with temperature, reaching 5.5%, 32.2%, and 52.2% at 30, 60, and 90 °C, respectively. However, a higher temperature will result in the over-hydrogenation of cyclohexanone to cyclohexanol (up to 98.3% at 90 °C); thus, 60 °C is the optimal temperature for maintaining high selectivity toward cyclohexanone. Given the cascade nature of phenol hydrogenation, both conversion and product distribution are sensitive to hydrogen pressure. As shown in Fig. 3(c), increasing the hydrogen pressure (20% H_2/N_2) from 0.1 to 2.0 MPa markedly enhanced phenol conversion from 7.7% to 64.8%. Nevertheless, excessive pressure (2.0 MPa) favored further hydrogenation to cyclohexanol (93.6%); thus, 1.0 MPa is selected as the optimal hydrogen pressure. The influence of solvent polarity was also systematically investigated (Fig. 3(d)). Although the selectivity toward cyclohexanone remains consistently above 97.5% across all tested solvents, phenol conversion was negatively correlated with solvent polarity. The highest conversion (68.8%) was achieved in nonpolar n-hexane. These variations in catalytic performance likely arise from the differences in substrate and hydrogen solubility, catalyst dispersion, and substrate adsorption and product desorption behaviors on the catalyst surface. Contact angle measurement (Fig. S15 in the ESM) reveals that the hydrophobic surface of Pd-$PMo_{10}V_2$, induced by surface-bound OA/OAm molecules, exhibits a water contact angle of ~ 114.7°, which may further influence the reaction microenvironment at the solid–liquid interface.

The influence of different POMs on selective phenol hydrogenation was also investigated. As shown in Fig. 3(e), the types of POMs have a negligible impact on the product selectivity, with all Pd–POM catalysts exhibiting cyclohexanone selectivity exceeding 97%. However, notable differences are observed in the catalytic activity. For instance, Pd-PW_{12} displays minimal phenol conversion (1.9%) within 3 h whereas Pd-PMo_{12} achieves a markedly higher conversion of 29.8%, representing a ~ 15-fold increase. This enhancement is amplified upon the partial substitution of Mo with V in $PMo_{12-x}V_x$ clusters. The phenol conversions reach 56.0%, 68.4%, and 50.1% for Pd-$PMo_{11}V_1$, Pd-$PMo_{10}V_2$, and Pd-PMo_9V_3, respectively. For better comparison, the turnover frequency (TOF) values of different catalysts were evaluated based on the ICP-AES results. As shown in Fig. S16 in the ESM, the TOF values are consistent with the catalytic performance, with Pd-$PMo_{10}V_2$ demonstrating a much higher value (11.0 h^{-1}) than Pd-PW_{12} (0.4 h^{-1}) and Pd-PMo_{12} (7.5 h^{-1}). Variations in activity among these V-substituted catalysts are attributed to differences in their redox behaviors, particularly the valence states and redox potentials of V atoms within the POMs. The synthesized hybrid catalysts were also compared with commercial Pd/C catalysts (5 wt.%) in terms of hydrogenation performance. As shown in Figs. S17 and S18 in the ESM, 5% Pd/C only converts 36.7%, which is much lower than the 68.8% of Pd-$PMo_{10}V_2$ under the same reaction conditions. The time–conversion–selectivity profiles for Pd-$PMo_{11}V_1$, Pd-$PMo_{10}V_2$, and Pd-PMo_9V_3 are shown in Fig. 3(f) and Fig. S19 in the ESM. All catalysts exhibit progressive phenol conversion over 5 h, with high cyclohexanone selectivity

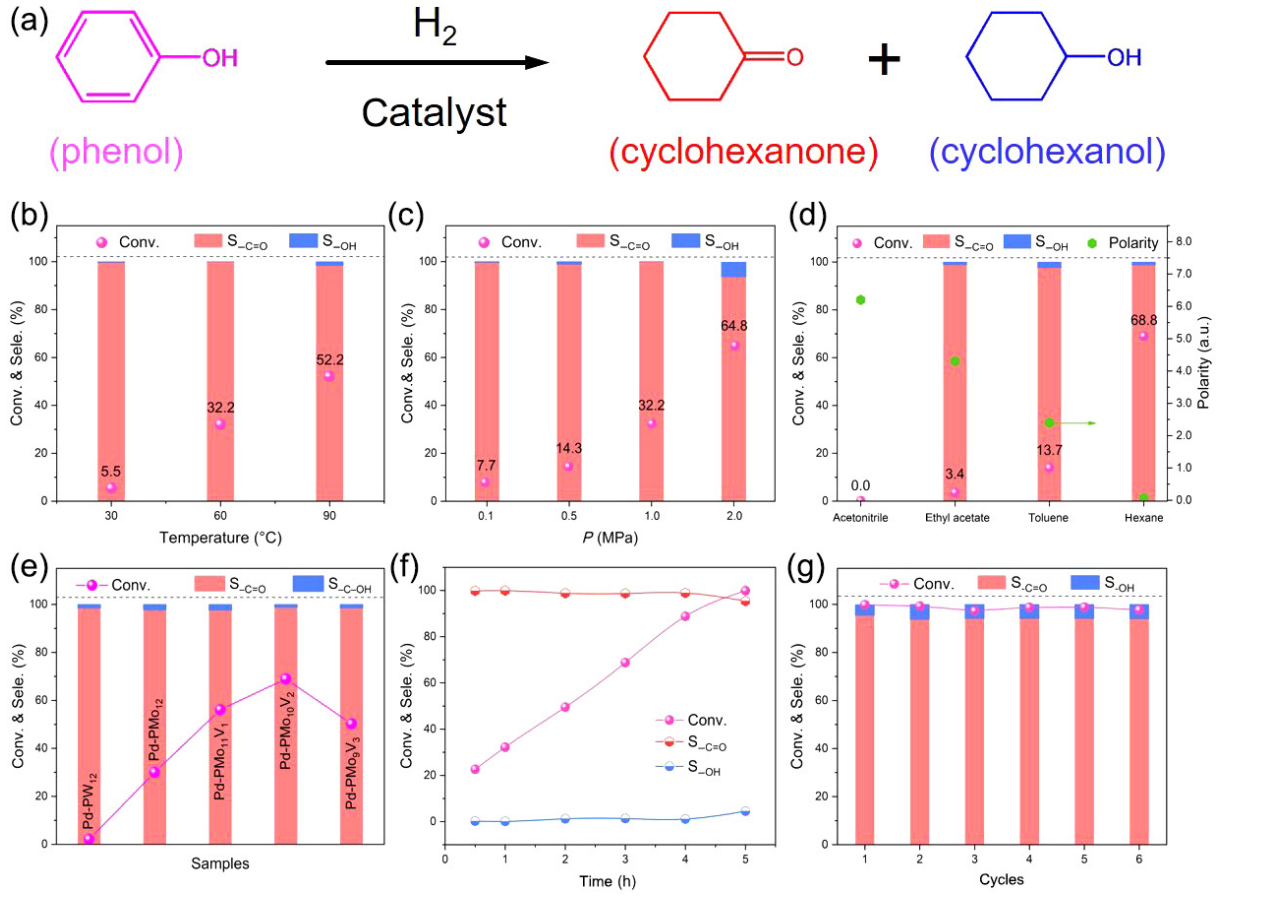

Figure 3 (a) The diagram route of phenol selective hydrogenation. The effects of (b) temperature, (c) pressure, (d) solvent polarity on the catalytic performance of Pd-$PMo_{10}V_2$. (e) The catalytic performance of different catalysts. (f) The time–conversion–selectivity curves and (g) the cycling result of phenol hydrogenation of Pd-$PMo_{10}V_2$.

maintained (above 95%) even at full conversion, despite minor cyclohexanol formation. Notably, Pd-$PMo_{10}V_2$ exhibits excellent cycling stability, retaining both activity and selectivity over six consecutive cycles without apparent deactivation (Fig. 3(g)). Moreover, the catalytic performance of Pd-$PMo_{10}V_2$ was compared with the reported literature, which demonstrates its superior phenol conversion performance (Table S4 in the ESM). Post-reaction characterizations (including XRD, FTIR, TEM, and ICP analyses) confirm that the structural integrity, elemental composition, and morphological features of Pd-$PMo_{10}V_2$ remain essentially unaltered, validating its superior durability under the reaction conditions (Figs. S20–S22 and Table S2 in the ESM).

The catalytic efficiency of Pd-$PMo_{10}V_2$ for the selective hydrogenation of phenol and its derivatives was also evaluated under the optimized reaction conditions (Table S5 in the ESM). Pd-$PMo_{10}V_2$ demonstrates excellent activity, achieving near-complete conversion (up to 99.9%) and high selectivity toward the corresponding ketones across a range of substituted phenols. Notably, the introduction of methyl substituents on the aromatic ring results in a moderate decline in conversion, attributable to the increased steric hindrance that impedes substrate adsorption and subsequent hydrogenation on the catalyst surface. Nevertheless, Pd-$PMo_{10}V_2$ maintains robust performance across structurally diverse substrates, highlighting its broad substrate compatibility and promising applicability in the selective transformation of phenolic compounds to ketones. These results underscore its potential for practical application in fine chemical synthesis and industrial-scale catalytic hydrogenation processes.

3.3 Mechanism investigation of selective hydrogenation

To elucidate the catalytic mechanism, the chemical valence states of key elements in Pd-$PMo_{10}V_2$ before and after reaction were investigated via XPS measurements. As shown in Fig. S23 in the ESM, the XPS survey spectra confirm the presence of C, N, O, P, V, Mo, and Pd in fresh and used catalysts, indicating excellent structural and compositional stability. The high-resolution Pd 3d spectra in Fig. 4(a) reveal an increase in the proportion of metallic Pd^0 species from 72.4% to 82.8% after the reaction, suggesting enhanced hydrogen adsorption and activation capability, which is beneficial for catalytic performance. In addition, the high-resolution V $2p_{3/2}$ spectra show a substantial increase in the V^{4+} content from 23% to 51%, indicating a partial reduction of vanadium centers during the reaction (Fig. 4(b)). A similar trend is observed in the high-resolution Mo 3d spectra, where the proportion of reduced Mo species increases from 3.7% to 10.6% (Fig. 4(c) and Table S6 in the ESM). These results imply that the POMs serve as an electron/proton reservoir, capable of accepting activated hydrogen species generated on the Pd clusters. This dynamic redox interplay facilitates efficient electron-coupled proton ($e^- + H^+$) transfer during catalysis without compromising the structural integrity of $PMo_{10}V_2$ [36].

The activation, diffusion, and transfer of H_2 on the catalyst

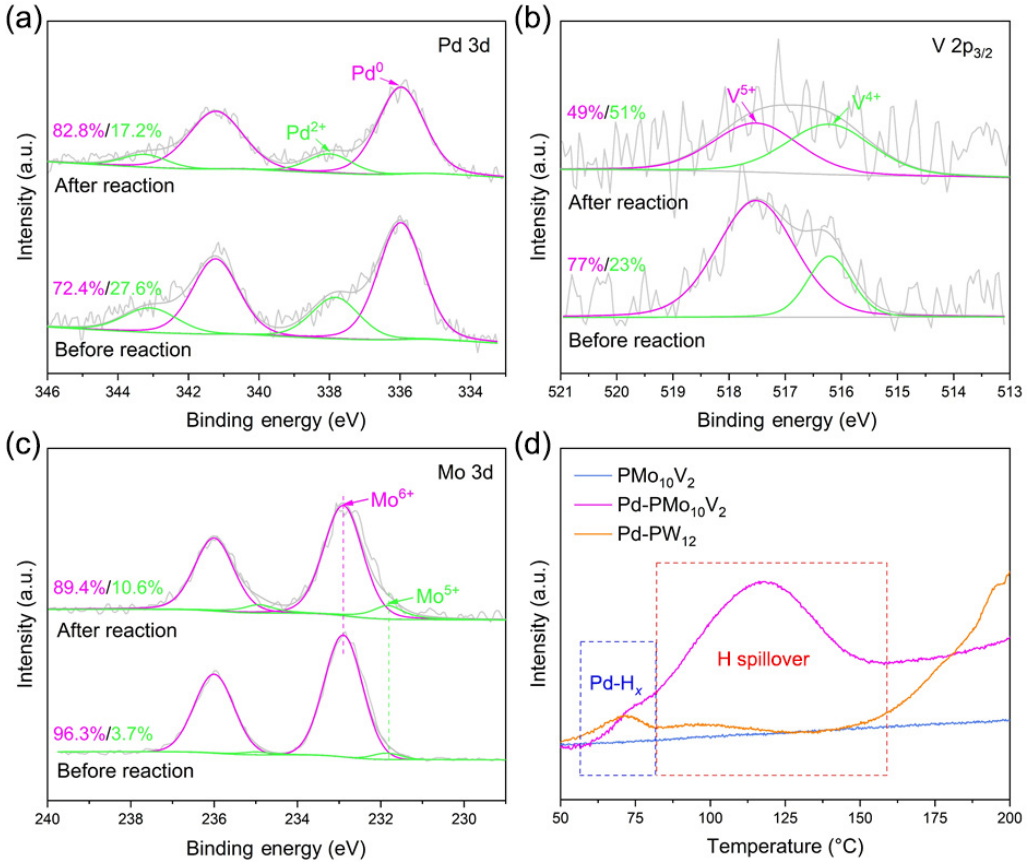

Figure 4 High-resolution XPS spectra of (a) Pd 3d, (b) V $2p_{3/2}$ and (c) Mo 3d before and after reaction. (d) H_2-TPD curves of $PMo_{10}V_2$, Pd-PW_{12} and Pd-$PMo_{10}V_2$, respectively.

surface are crucial for the subsequent hydrogenation process [56], which is revealed by H_2-TPD experiments over the temperature range of 50–200 °C (Fig. 4(d)). No discernible H_2 desorption peak is observed in $PMo_{10}V_2$, indicating that pristine POMs lack the intrinsic ability to activate and dissociate H_2 molecules. Meanwhile, two distinct desorption peaks are detected for Pd-PW_{12} and Pd-$PMo_{10}V_2$ at ~ 72 °C and 80–150 °C, attributable to the desorption of surface-adsorbed active hydrogen species and hydrogen spillover from Pd clusters to POMs, respectively [36, 57]. Notably, the peak intensities of Pd-$PMo_{10}V_2$ are much higher than those of Pd-PW_{12}, likely due to the presence of a greater quantity of active Pd species and the inherently lower redox potential of $PMo_{10}V_2$, which facilitates the acceptance of both electrons and dissociated hydrogen species. A WO_3-based colorimetric assay, wherein yellow WO_3 can undergo a visible color change to dark green tungsten bronze upon interaction with active hydrogen species ($WO_3 + H_2 \rightarrow H_xWO_3$), was employed to validate the occurrence of H spillover [11]. As shown in Fig. S24(a) in the ESM, pristine WO_3 retains its color after exposure to H_2, confirming its inability to activate H_2 independently. However, when WO_3 is mixed with Pd-$PMo_{10}V_2$ and treated with H_2 (Fig. S24(b) in the ESM), a pronounced color change to blue is observed, indicating effective hydrogen spillover and supporting the superior H_2 activation and dissociation capability of Pd-$PMo_{10}V_2$, consistent with the H_2-TPD findings.

Based on the above comprehensive analysis, a plausible reaction mechanism for the selective hydrogenation of phenol over Pd–POM cluster catalysts was proposed (Scheme 1). Initially, H_2 molecules are adsorbed and dissociated on the surface of ultra-small Pd clusters, generating active hydrogen species. Subsequently, these

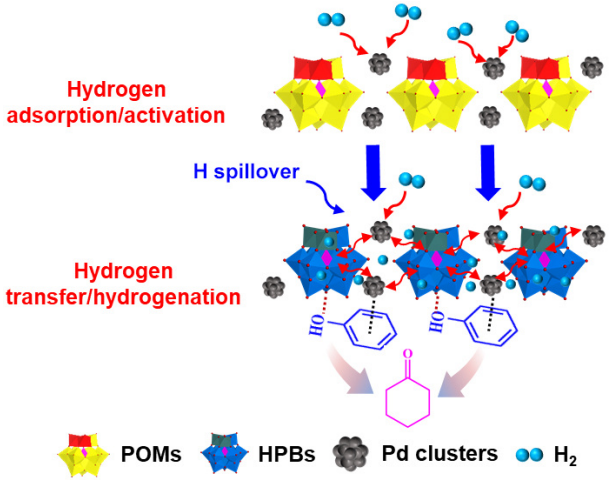

Scheme 1 Schematic diagram of possible reaction mechanism for selective hydrogenation of phenol on Pd-POMs cluster catalyst.

species migrate to adjacent POMs via a hydrogen spillover process to form heteropoly blue species. At present, phenol molecules are activated through dual-site adsorption: The hydroxyl group forms hydrogen bonds with the oxygen-rich surface of POMs, whereas the aromatic ring interacts with neighboring Pd clusters to undergo a hydrogenation reaction. According to previous characterizations, the modulation of the redox properties of POMs (particularly via vanadium substitution in $PMo_{12-x}V_x$) markedly enhances the extent of hydrogen spillover, thereby improving the overall hydrogen availability for the catalytic cycle. Moreover, the energy barrier

associated with the back-transfer of activated hydrogen from POMs to Pd sites is mitigated at high temperatures, contributing to the observed improvement in catalytic performance.

4 Conclusion

In summary, a series of cluster catalysts was successfully constructed through the self-assembly of sub-nanometer Pd^0 clusters and various POMs. Up to five distinct types of POMs were explored, among which Pd-$PMo_{10}V_2$ exhibits the most outstanding catalytic performance in the selective hydrogenation of phenol to cyclohexanone. Under optimized conditions (60 °C and 1.0 MPa of 20% H_2/N_2), Pd-$PMo_{10}V_2$ can achieve a phenol conversion of 99.9% with a cyclohexanone selectivity of 95.4% while maintaining its structural integrity and catalytic stability over six consecutive cycles. The superior performance is attributed to the synergistic integration of POMs and Pd clusters: Sub-nano Pd clusters act as active sites for H_2 activation and dissociation, whereas POMs not only stabilize the Pd species but also function as electron/hydrogen acceptors via the spillover effect. This dual functionality effectively enhances the reactive hydrogen concentration and active sites. Further, experimental results indicate that a moderate increase in the reaction temperature facilitates the release and use of stored hydrogen species from POMs, thereby promoting the hydrogenation process. This work offers a promising strategy for the rational design of noble-metal cluster-based catalysts with enhanced activity and selectivity, paving the way for advanced applications in selective hydrogenation reactions.

Electronic Supplementary Material: Supplementary material (including TEM images, FTIR, XRD of the comparison catalysts, the TGA, XPS, ICP and the TOF values of catalysts) is available in the online version of this article at https://doi.org/10.26599/POM.2026.9140109.

Date availability

All data needed to support the conclusions in the paper are presented in the manuscript and the Electronic Supplementary Material. Additional data related to this paper may be requested from the corresponding author upon request.

Acknowledgements

The authors gratefully acknowledge the financial support from the National Natural Science Foundation of China (Nos. 22471030, 22171041, and 22379024), Natural Science Foundation of Jilin Province Science and Technology Department (discipline layout project) (No. 20250102064JC), and Postdoctoral Fellowship Program of CPSF (No. GZC20250674).

Declaration of competing interest

The authors have no competing interests to declare that are relevant to the content of this article. Author Yangguang Li is the Associate Editor of this journal, but he is not involved in the peer-review or decision of this article.

Author contribution statement

Y. C. L.: Writing – original draft, investigation, conceptualization. Z. X. L.: Writing – original draft, investigation, conceptualization. Z. L. L.: Writing – review & editing, investigation, funding acquisition. R. Q. Y.: Investigation, conceptualization. F. Y. Y.: Investigation, conceptualization. A. C. L.: Investigation, conceptualization. H. Q. T.: Writing – review & editing, investigation, funding acquisition. Y. G. L.: Writing – review & editing, investigation, funding acquisition.

Use of AI statement

During the preparation of this work, the authors used Chatgpt to revise the manuscript. After using this tool, the authors reviewed and edited the content as needed and took full responsibility for the content of the publication.

References

[1] Wang, X. C.; Xiao, T. T.; Liu, Y. C.; Zhang, C.; Zhao, F. Y. Heterolytic hydrogenation and H^- migration-assisted hydrodeoxygenation reaction under mild conditions over Pt/TiO_2-D. *ACS Catal.* **2024**, *14*, 13800–13813.

[2] Wu, X. J.; Fan, X. T.; Xie, S. J.; Lin, J. C.; Cheng, J.; Zhang, Q. H.; Chen, L. Y.; Wang, Y. Solar energy-driven lignin-first approach to full utilization of lignocellulosic biomass under mild conditions. *Nat. Catal.* **2018**, *1*, 772–780.

[3] Xiao, T. T.; Li, J. R.; Li, J.; Gong, Q. H.; Luo, P. K.; Su, X. L. N.; Cheng, H. Y.; Zhang, C.; Zhao, F. Y. Efficient hydrogenolysis of C–O bond over Pd/P–TiO_2: The generation and role of brønsted acid site triggered by spillover hydrogen. *ACS Catal.* **2025**, *15*, 2222–2235.

[4] Zeng, Y.; Zhao, M. T.; Zeng, H. L.; Jiang, Q.; Ming, F. W.; Xi, K.; Wang, Z. C.; Liang, H. F. Recent progress in advanced catalysts for electrocatalytic hydrogenation of organics in aqueous conditions. *eScience* **2023**, *3*, 100156.

[5] Zhao, H. P.; Du, X. Q. Polyoxometalates as the redox anolyte for efficient conversion of biomass to formic acid. *Chin. J. Struct. Chem.* **2024**, *43*, 100246.

[6] Wang, X. C.; Arai, M.; Wu, Q. F.; Zhang, C.; Zhao, F. Y. Hydrodeoxygenation of lignin-derived phenolics-a review on the active sites of supported metal catalysts. *Green Chem.* **2020**, *22*, 8140–8168.

[7] Li, G. F.; Han, J. Y.; Wang, H.; Zhu, X. L.; Ge, Q. F. Role of dissociation of phenol in its selective hydrogenation on Pt(111) and Pd(111). *ACS Catal.* **2015**, *5*, 2009–2016.

[8] Zhang, M. Y.; Li, Y. Z.; Gupta, R. K.; Lou, M. J.; Jiang, Y. S.; Li, Z.; Zhang, Y. L.; Zhang, J. Y.; Huang, X. Q.; Zhang, Q. D. et al. Recent advances in polyoxometalates-based photocatalysts for sustainable selective organic transformation. *Chin. Chem. Lett.*, in press, https://doi.org/10.1016/j.cclet.2025.111897.

[9] Liu, Y. N.; Meng, Q. L.; Zhang, K. L.; Han, W. Y.; Zheng, X. R.; Wang, Y. Q.; Han, Y. B.; Wang, J. P.; Wu, H. H.; He, M. Y. et al. Selective hydrogenation of phenols to cyclohexanones over hydrotalcite-supported Pd single-atom catalyst. *Angew. Chem., Int. Ed.* **2025**, *64*, e202504260.

[10] Liu, Y. B.; Ji, K. Y.; Wang, X.; Shi, Q. J.; Li, A. Z.; Yin, Z. Q.; Zhu, Y. Q.; Duan, H. H. Modulating the coverage of adsorbed hydrogen via hydrogen spillover enables selective electrocatalytic hydrogenation of phenol to cyclohexanone. *Angew. Chem., Int. Ed.* **2024**, *64*, e202419178.

[11] Ding, X. L.; Gao, R. Y.; Chen, Y.; Wang, H. Y.; Liu, Y. D.; Zhou, B. H.; Wang, C. F.; Bai, G. M.; Qiu, W. G. Carbon vacancies in graphitic carbon nitride-driven high catalytic performance of Pd/CN for phenol-selective hydrogenation to cyclohexanone. *ACS Catal.* **2024**, *14*, 3308–3319.

[12] Liu, H. Z.; Jiang, T.; Han, B. X.; Liang, S. G.; Zhou, Y. X. Selective phenol hydrogenation to cyclohexanone over a dual supported Pd-

Lewis acid catalyst. *Science* **2009**, *326*, 1250–1252.
[13] Zhou, P.; Guo, S. X.; Li, L. B.; Ueda, T.; Nishiwaki, Y.; Huang, L.; Zhang, Z. H.; Zhang, J. Selective electrochemical hydrogenation of phenol with earth-abundant Ni–MoO_2 heterostructured catalysts: Effect of oxygen vacancy on product selectivity. *Angew. Chem., Int. Ed.* **2023**, *62*, e202214881.
[14] Lin, C. J.; Huang, S. H.; Lai, N. C.; Yang, C. M. Efficient room-temperature aqueous-phase hydrogenation of phenol to cyclohexanone catalyzed by Pd nanoparticles supported on mesoporous MMT-1 silica with unevenly distributed functionalities. *ACS Catal.* **2015**, *5*, 4121–4129.
[15] Wei, H. H.; Shao, S. X.; Deng, B. H.; Xue, Y. F.; Chen, W. X.; Yin, L. L.; Lin, Y. X.; Hussain, N.; Wu, X. D.; Ge, B. H. et al. Generalized rapid synthesis of supported nanocluster catalyst for mild hydrogenation of phenol toward KA oil. *Small* **2023**, *19*, 2207759.
[16] Huang, X. B.; Li, X. Y.; Xia, W.; Hu, B.; Muhler, M.; Peng, B. X. Highly dispersed Pd clusters/nanoparticles encapsulated in MOFs via *in situ* auto-reduction method for aqueous phenol hydrogenation. *J. Mater. Sci. Technol.* **2022**, *109*, 167–175.
[17] Wu, S.; Zhao, C. C.; Dong, Y. J.; Yan, L. K. Cyclohexanone hydrogenation to cyclohexanol on phosphomolybdate supported Pt single-atom catalyst: A density functional theory study. *Polyoxometalates* **2024**, *3*, 9140070.
[18] Sanwal, P.; Raza, A.; Miao, Y. X.; Lumbers, B.; Li, G. Advances in coinage metal nanoclusters: From synthesis strategies to electrocatalytic performance. *Polyoxometalates* **2024**, *3*, 9140057.
[19] Liu, Y. C.; Zhou, X. G.; Qiu, T. Y.; Yao, R. Q.; Yu, F. Y.; Song, T. T.; Lang, X. Y.; Jiang, Q.; Tan, H. Q.; Li, Y. Q. et al. Co‐assembly of polyoxometalates and porphyrins as anode for high‐performance lithium‐ion batteries. *Adv. Mater.* **2024**, *36*, 2407705.
[20] Yang, G. P.; Liu, Y. F.; Wei, Y. G. Application of polyoxometalates in biomass conversion. *Coord. Chem. Rev.* **2024**, *521*, 216172.
[21] Chen, X. F.; Li, Q. Q.; Li, M. J.; Shi, M. J.; Liang, M. Q.; Chen, Y. F.; Bai, F.; Lan, Y. Q. Frontiers in polyoxometalate‐based hybrids for photothermal catalysis. *Adv. Funct. Mater.*, in press, DOI: 10.1002/adfm.202510863.
[22] Zang, D. J.; Wang, H. Q. Polyoxometalate-based nanostructures for electrocatalytic and photocatalytic CO_2 reduction. *Polyoxometalates* **2022**, *1*, 9140006.
[23] Fu, K. W.; Liu, L.; Cui, P. C.; Yan, X. J.; Wang, Y. Y.; Chen, K. Polyoxometalate hybrid comb-like crosslinked polymer networks for anhydrous proton conductors. *Polyoxometalates* **2025**, *4*, 9140100.
[24] Huang, X. Q.; Liu, S.; Liu, G.; Tao, Y. W.; Wang, C. R.; Zhang, Y. L.; Li, Z.; Wang, H. W.; Zhou, Z.; Shen, G. D. et al. An unprecedented 2-fold interpenetrated open framework built from Zn_6 ring seamed trivacant polyoxotungstates used for photocatalytic synthesis of pyridine derivatives. *Appl. Catal. B: Environ.* **2023**, *323*, 122134.
[25] Liu, G.; Chen, Y. F.; Chen, Y. L.; Shi, Y. Q.; Zhang, M. Y.; Shen, G. D.; Qi, P. F.; Li, J. K.; Ma, D. L.; Yu, F. et al. Indirect electrocatalysis S–N/S–S bond construction by robust polyoxometalate based foams. *Adv. Mater.* **2023**, *35*, 2304716.
[26] Hu, Q. L.; Li, K.; Chen, X. J.; Liu, Y. F.; Yang, G. P. Polyoxometalate catalysts for the synthesis of N-heterocycles. *Polyoxometalates* **2024**, *3*, 9140048.
[27] Zhang, X. Y.; Li, H.; Xu, N.; Liu, X. D.; Wang, X. L. Engineering geometric metamorphosis in $\{P_6M_2Mo_{16}O_{73}\}$-based high-nuclearity metal superclusters: From tetrahedral to square assemblies via topological transformations. *Inorg. Chem. Front.* **2025**, *12*, 3823–3832.
[28] Liu, Q. D.; He, S. Q.; Yu, B.; Cheng, X. J.; Shi, W. X.; Wang, X. Visible light induced Ag-polyoxometalate coassembly into single‐cluster nanowires. *Adv. Mater.* **2022**, *34*, 2206178.
[29] Liu, J. L.; Wang, S. B.; Liu, N.; Yang, D. R.; Wang, H. W.; Hu, H. S.; Zhuang, J.; Wang, X. Au-polyoxometalates A-B-A-B type copolymer-analogue sub-1 nm nanowires. *Small* **2021**, *17*, 2006260.
[30] Ge, H. Y.; Shi, W. X.; Liu, J. L.; Zhang, Y.; Wang, X. High Entropy oxide-polyoxometalate sub-1 nm hetero-nanowires as cathode catalysts in Li–O_2 batteries. *J. Am. Chem. Soc.* **2025**, *147*, 8367–8376.
[31] Zhang, F. H.; Shi, W. X.; Liu, Q. D.; Wang, X. Modular assembly of polyoxometalate clusters at the sub-1 nm scale. *Nat. Protoc.*, in press, DOI: 10.1038/s41596-025-01212-1.
[32] Zang, D. J.; Li, Q.; Dai, G. Y.; Zeng, M. Y.; Huang, Y. C.; Wei, Y. G. Interface engineering of Mo_8/Cu heterostructures toward highly selective electrochemical reduction of carbon dioxide into acetate. *Appl. Catal. B: Environ.* **2021**, *281*, 119426.
[33] Gao, Z. Y.; Yu, F.; Zhang, M. Y.; Huang, X. Q.; Fu, S. Q.; Azam, M.; Shen, G. D.; Yao, Q. X.; Zhang, Q. D.; Chen, Y. F. et al. Molecular junction polyoxotungstate-based copper-organic frameworks for photocatalytic cross-dehydrogenative coupling. *Angew. Chem., Int. Ed.* **2025**, *64*, e202516079.
[34] Yang, G. P.; Lin, Z. F.; Zhang, X. Z.; Cao, J. W.; Chen, X. J.; Liu, Y. F.; Lin, X. L.; Li, K. Assembly of Y(III)-containing antimonotungstates induced by malic acid with catalytic activity for the synthesis of imidazoles. *Chin. Chem. Lett.* **2024**, *35*, 110274.
[35] Yang, G. P.; Liu, H. Q.; Chen, J. C.; Lin, X. L.; Tan, K. X.; Dong, Y. Y.; Liu, Y. F.; Wei, Y. G. Dy/Ho-encapsulated tartaric acid-functionalized tungstoantimonates: Heterogeneous catalysts for isoindolinone synthesis. *Chem. Commun.* **2024**, *60*, 10934–10937.
[36] Liu, Y. C.; Wang, X. C.; Lang, Z. L.; Li, Y. Q.; Yu, F. Y.; Dong, H. L.; Yao, R. Q.; Geng, S.; Liu, Z. X.; Tan, H. Q. et al. Pd^0-polyoxometalates cluster-cluster catalyst for efficient selective hydrogenation of olefins. *Nano Res.* **2025**, *18*, 94907437.
[37] Hülsey, M. J.; Fung, V.; Hou, X. D.; Wu, J. S.; Yan, N. Hydrogen spillover and its relation to hydrogenation: Observations on structurally defined single-atom sites. *Angew. Chem. Int. Ed.* **2022**, *61*, e202208237.
[38] Li, S. J.; Ma, Y. B.; Zhao, Y.; Liu, R. J.; Zhao, Y. P.; Dai, X. S.; Ma, N. N.; Streb, C.; Chen, X. N. Hydrogenation catalysis by hydrogen spillover on platinum‐functionalized heterogeneous boronic acid‐polyoxometalates. *Angew. Chem., Int. Ed.* **2023**, *62*, e202314999.
[39] Li, S. J.; Huang, M. Y.; Cheng, W. Y.; Shah, W. A.; Dai, X. S.; Ma, N. N.; Zhao, Q. Y.; Chen, X. N. An unprecedented oxalate-functionalized Ta/W polyoxometalate enabling the self-assembly of a 2D composite for catalytic hydrogenation. *Inorg. Chem. Front.* **2024**, *11*, 7324–7332.
[40] Wang, Q.; Wang, G. N.; Ren, H. Y.; Li, Z. H.; Zhang, C. J.; Chen, T. T.; Pang, H. J. Polyoxometalate-based materials for electrochemical energy storage and catalytic hydrogen production. *Coord. Chem. Rev.* **2025**, *545*, 217044.
[41] Zhang, M. X.; Peng, J. H.; Zhang, Z.; Ma, X. J.; Xing, S. Z.; Liu, Y. W. Electron-deficient defect sites in polyoxometalate-based metal-organic frameworks induced by atom substitution-modulated host-guest interaction. *Sci. Bull.* **2025**, *70*, 1986–1993.
[42] Cao, J. W.; Jiao, L. Y.; Zhang, F. H.; Wang, H. Z.; Xia, W. Q.; Cao, X. H.; Yang, G. P. Dual-ligand-regulated Tb-containing antimonotungstate for the heterogeneous catalytic synthesis of N-heterocycles in ethanol. *Inorg. Chem.* **2025**, *64*, 13157–13162.
[43] Tsigdinos, G. A.; Hallada, C. J. Molybdovanadophosphoric acids and their salts. *I. Investigation of methods of preparation and characterization. Inorg. Chem.* **1968**, *7*, 437–441.
[44] Liu, Y. C.; Zhu, C. Y.; Zhao, X.; Tan, H. Q.; Cheng, S. H.; Yang, D.; Wang, X.; Li, Y. G. $CdWO_4$ sub-1 nm nanowires for visible-light CO_2 photoreduction. *Angew. Chem., Int. Ed.* **2025**, *64*, e202418349.
[45] Tang, W. S.; Zhang, L. N.; Qiu, T. Y.; Tan, H. Q.; Wang, Y. H.; Liu, W.; Li, Y. G. Efficient conversion of biomass to formic acid coupled with low energy consumption hydrogen production from water electrolysis. *Angew. Chem., Int. Ed.* **2023**, *62*, e202305843.
[46] Zhang, R.; Liu, Z. L.; Zheng, S. H.; Wang, L. Q.; Zhang, L.; Qiao, Z. A. Pyridinic nitrogen sites dominated coordinative engineering of subnanometric Pd clusters for efficient alkynes' semihydrogenation. *Adv. Mater.* **2023**, *35*, 2209635.

[47] Yu, B.; Xiu, Y.; Zhang, S. M.; Wang, X. Polymer-like photochromic tungsten oxide sub-1 nm nanowires. *J. Am. Chem. Soc.* **2025**, *147*, 26626–26634.
[48] Wang, J. J.; Wu, Z. Y.; Li, Q.; Zhang, H. L.; Liu, Y.; Ji, G. X.; Zhang, Y. L.; Li, Q. L.; Ren, J. Y.; Zhang, Q. D. et al. Engineering boron-imidazolate-based polyoxometalates for photooxidative C=C bond cleavage in aqueous media. *Polyoxometalates* **2025**, *4*, 9140087.
[49] Predoeva, A.; Damyanova, S.; Gaigneaux, E. M.; Petrov, L. The surface and catalytic properties of titania-supported mixed PMoV heteropoly compounds for total oxidation of chlorobenzene. *Appl. Catal. A: Gen* **2007**, *319*, 14–24.
[50] Guo, R. C.; Zeng, Y. J.; Lin, L.; Hu, D.; Lu, C. Q.; Conroy, S.; Zhang, S. Y.; Zeng, C.; Luo, H. X.; Jiang, Z. W. et al. CO_2 - assisted controllable synthesis of PdNi nanoalloys for highly selective hydrogenation of biomass-derived 5-hydroxymethylfurfural. *Angew. Chem., Int. Ed.* **2025**, *64*, e202418234.
[51] Li, Z.; Zhang, J. H.; Jing, X. T.; Dong, J.; Liu, H. F.; Lv, H. J.; Chi, Y. N.; Hu, C. W. A polyoxometalate@covalent triazine framework as a robust electrocatalyst for selective benzyl alcohol oxidation coupled with hydrogen production. *J. Mater. Chem. A* **2021**, *9*, 6152–6159.
[52] Li, X. H.; Chen, W. L.; Tan, H. Q.; Li, F. R.; Li, J. P.; Li, Y. G.; Wang, E. B. Reduced state of the graphene oxide@polyoxometalate nanocatalyst achieving high-efficiency nitrogen fixation under light driving conditions. *ACS Appl. Mater. Interfaces* **2019**, *11*, 37927–37938.
[53] Wang, F.; Jing, C. J.; Ping, J. J.; He, D. Y.; Shang, W. H.; Zeng, M. L.; Wang, N.; Jia, Z. Y. Polyoxometalate-based Cu(II) complexes as the photocatalyst for oxidation of toluene and photodegradation of metronidazole. *Polyoxometalates* **2024**, *3*, 9140067.
[54] Hartnett, A. C.; Evenson, R. J.; Thorarinsdottir, A. E.; Veroneau, S. S.; Nocera, D. G. Lanthanum-promoted electrocatalyst for the oxygen evolution reaction: Unique catalyst or oxide deconstruction? *J. Am. Chem. Soc.* **2025**, *147*, 1123–1133.
[55] Zhang, H. C.; Yi, Z. D.; Fu, S. Y.; Li, C. Z.; Lucia, L. A.; Liu, Q. Y. Pd nanocubes supported on SiW_{12}@Co-ZIF nanosheets for high-efficiency rupture of ether bonds in model and actual lignin. *Appl. Catal. B: Environ.* **2023**, *322*, 122128.
[56] Fan, S. R.; Yao, Z. H.; Cheng, W.; Zhou, X.; Xu, Y.; Qin, X. T.; Yao, S. Y.; Liu, X.; Wang, J. G.; Li, X. N. et al. Subsurface Ru-triggered hydrogenation capability of TiO_{2-x} overlayer for poison-resistant reduction of *N*-heteroarenes. *ACS Catal.* **2023**, *13*, 757–765.
[57] Wu, P. Y.; Zhao, D. X.; Lu, G. P.; Cai, C. Supported Pd–Au bimetallic nanoparticles as an efficient catalyst for the hydrodeoxygenation of vanillin with formic acid at room temperature. *Green Chem.* **2022**, *24*, 1096–1102.

Yanchun Liu obtained his Ph.D. degree from Northeast Normal University (NENU) in 2024 with the supervision of Prof. Yangguang Li. Now, he work as a postdoctoral with Prof. Xun Wang in the Tsinghua University. His main research interest is concentrated on the design and assembly of POM-based subnano materials for energy and catalytic application.

Zixuan Liu is currently an undergraduate student at Northeast Normal University (NENU). His research focuses on the synthesis and characterization of polyoxometalates (POM)-based catalysts, with an emphasis on investigating the synergistic effects between metal clusters and polyoxometalates to improve catalytic efficiency in the selective conversion of lignin-derived platform molecules.

Zhongling Lang obtained her M.S. degrees at Northeast Normal University (NENU) in China in 2013. In 2014, she joined the Quantum Chemistry Group at the Rovira i Virgili University (Tarragona). She received her Ph.D. on the electronic properties of polyoxometalates under the supervision of Prof. Josep M. Poblet and Dr Anna Clotet in 2017. Since 2017, She started his research in NENU. Her research activity concerns the application of computational methods to the study transition metal-based molecular systems with special interest in energy conversion area.

Ruiqi Yao received her Bachelor's and Ph.D. degree in Engineering (through a combined Master–Ph.D. program) from Jilin University, under the supervision of Professors Qing Jiang and Xingyou Lang. She is currently working at Northeast Normal University (NENU) in Yangguang Li's group, where her research focuses on the synthesis of nanoporous metals and polyoxometalate-based metal composite materials as well as their applications in green electrosynthesis.

Feiyang Yu is now as an associated Professor at Northeast Normal University (NENU). She received the Ph.D. degree from NENU in 2021. She worked as a post PhD. at Macao Institute of Materials Science and Engineering of Macau University of Science and Technology. Her current research interest is concentrated on polyoxometalate and polyoxometalate (POM)-based composites for electrochemical application.

Aicen Li is currently pursuing her Ph.D. degree in Inorganic Chemistry at Northeast Normal University (NENU). Her research primarily focuses on the design, synthesis and property exploration of functional cluster-based covalent organic framework (COF) materials, aiming to develop novel multifunctional material systems.

Huaqiao Tan received Ph.D. degree from Northeast Normal University (NENU) in 2012 with the supervision of Prof. Enbo Wang. Later, he worked as a "Hong Kong Scholars" (2019) with Prof. Wing-Kei Ho in the Education University of Hong Kong. He has been a full professor at NENU since 2020. His main research interest is concentrated on the design and synthesis of inorganic nanostructures, polyoxometalates for energy and environmental catalysis.

Yangguang Li obtained his B.S., M.S. and Ph.D. degrees at Northeast Normal University (NENU) in China from 1993 to 2003. He then started his postdoc career at CNRS-CRPP in France and Karsluhe University in Germany from 2004 to 2006. He started his own research at NENU in China in 2007. His group's research is Polyoxometalate (POM) chemistry, especially concentrated on the photo- and electro-functional materials based on POM clusters towards the application of new energy area.